Finite-size effects in dislocation glide through random arrays of obstacles: Line tension simulations

Thomas Nogaret and David Rodney
Génie Physique et Mécanique des Matériaux (UMR CNRS 5010), Institut National Polytechnique de Grenoble, ENSPG, 101 Rue de la Physique, Saint Martin d'Hères Cedex Boîte Postale 46 38402, France
(Received 20 June 2006; published 23 October 2006)

The stress required to force a dislocation to glide through a random environment of obstacles depends on both the dislocation length and the glide distance because of the statistical nature of the obstacle configurations. In order to study this finite size effect, we employ a line tension model in conjunction with an evolution algorithm inspired from larger scale dislocation dynamics simulations. We show that with finite arrays, the estimated critical resolved shear stress is larger than its infinite array limit. Moreover, the lower the resistance and the density of the obstacles, the larger the overestimation. The controlling parameters, estimated from Friedel's law, are the average number of obstacles along the dislocation line and the average number of obstacle configurations met by the dislocation in its glide. We analyze this effect through a model based on an analogy with branching processes.

DOI: 10.1103/PhysRevB.74.134110 PACS number(s): 61.72.Bb, 62.20.Fe

I. INTRODUCTION

There are classical size effects in metallurgy. One of the most famous is the Hall Petch effect[1,2] which recognizes that the elastic limit of a polycrystal is inversely proportional to the square root of its mean grain size. But there are more subtle size effects. For example, it was recently observed in molecular dynamics (MD) simulations of the glide of an edge dislocation in a Ni(Al) random solid solution[3,4] that the critical resolved shear stress (CRSS) computed from the simulations decreased if the dislocation length was increased.

This observation can be *qualitatively* understood in the case of weak obstacles from the randomness of the configuration and the unzipping mechanism:[5] if an obstacle breaks along the dislocation line, the distance between its neighboring obstacles increases, weakening the latter and favoring new breaking events. An avalanche of breaking events thus propagates along the dislocation line, leading to its unpinning. The resistance on the dislocation is therefore controlled by the weakest pinning point along the line, and in a random obstacle configuration, the longer the dislocation, the higher the probability of finding widely spaced, i.e., weak, obstacles along the line, and consequently, the lower the CRSS. On the other hand, if the dislocation glide distance is increased, the probability of finding a stable configuration ahead of the dislocation that will pin the latter, is increased. Thus the CRSS decreases with increasing dislocation length and increases with increasing glide distance.

Our aim is to investigate *quantitatively* this finite size effect. In order to perform the large number of simulations on different random obstacle configurations required to obtain accurate statistics, we use the simplest dislocation model, i.e., the line tension model,[5] which assumes that a dislocation is an elastic string with a constant energy per unit length. Simulations based on the line tension model have first been used by Foreman and Makin[6] to study the glide of a dislocation in random arrays of point-obstacles of various resistances. In the limit of weak obstacles, their simulations showed a good agreement with Friedel's law [5] that is obtained by imposing that the number of obstacles on a gliding dislocation is stationary, yielding an average distance between obstacles on the dislocation line (l_F) larger than the average distance between obstacles in the glide plane (d) and equal to

$$l_F = \frac{d}{\sqrt{\cos(\phi_c/2)}}, \tag{1}$$

where ϕ_c is the critical breaking angle, characteristic of the obstacle resistance (see below for details). With the usual line tension relation between the CRSS and the distance between obstacles along the dislocation line $\tau_F = \cos(\phi_c/2)\mu b/l_F$ (μ is the shear modulus, b the magnitude of the Burgers vector), one obtains Friedel stress:

$$\tau_F = \cos(\phi_c/2)^{3/2}\mu\frac{b}{d}. \tag{2}$$

Two models were developed to deduce the CRSS from the statistics of stable dislocation configurations. Different techniques were used but led to similar results, predicting that for infinitely large arrays, the CRSS should be a fraction of Friedel stress:

$$\tau_\infty = \alpha\tau_F \tag{3}$$

with $\alpha=0.8871$ in the work of Hanson and Morris[7] and $\alpha=0.949$ in that of Labusch.[8] The former expression was found to reproduce line tension simulations for breaking angles ϕ_c from 180° [$\cos(\phi_c/2)=0$] down to about 145° [$\cos(\phi_c/2)=0.3$].[9] Mixtures of obstacles with different resistances have also been considered in line tension simulations[10] and more recently in an analytical model.[11]

In these various studies, finite size effects have not been discussed in detail since in the simulations, square cells with only one or two obstacle densities were employed, and in the models, arrays of arbitrarily large sizes were assumed. One exception is the expression of the CRSS obtained by La-

busch from dimensional arguments.[8] However, we show in the following that, as already pointed out in the case of square arrays,[12] although this expression correctly predicts the trends of the size effect, it is not quantitatively accurate.

It is to be noted that the linearized version of the line tension model has been extensively used to study the motion in random pinning media of charge density waves and flux lines in supraconductors.[13,14] The elastic limit at 0 K is then associated to a dynamical depinning transition. However, these authors have not studied size effects in detail either.

In the present paper, we perform a detailed study of the size effect in rectangular arrays of various aspect ratios in the case of weak obstacles where the unzipping mechanism prevails. We show that this size effect is most important for weak obstacles in low densities. In Sec. II, we present an algorithm developed to introduce dynamical effects in line tension simulations. The results of the simulations are detailed in Sec. III and analyzed in Sec. IV through a model based on an analogy with branching processes first proposed in Ref. 7.

II. COMPUTATIONAL MODEL

We describe here the algorithm used in conjunction with the line tension model. It is different from the geometrical *Circle Rolling* procedure used in the past[6,9,12] and was developed with the aim to incorporate dynamical effects in the line tension simulations. It is inspired from more accurate dislocation dynamics (DD) simulations.[15]

A. Configuration description

The simulations are two-dimensional, with the obstacles randomly positioned. In the following, stresses are normalized as $\tau^*=\tau d/\mu b$ and distances as $R^*=R/d$, where d is the average distance between obstacles in the plane, b the Burgers vector, and μ the shear modulus. The dislocation line tension is assumed to be $T=1/2\mu b^2$. The obstacles are characterized by their breaking angle ϕ_c, i.e., the angle that the dislocation makes around the obstacle when the latter breaks. The dislocation is defined by a sequence of consecutive segments $n_S n_F$ pinned between nonbroken obstacles, as shown schematically in Fig. 1. The segments bow out with a constant radius of curvature given by the line tension model: under the scaled stress τ^*, the radius of curvature is $R^*=1/2\tau^*$. The angles made by the dislocation around n_S and n_F are, respectively, noted ϕ_S and ϕ_F.

As illustrated in Fig. 1, a pinned segment can evolve in three distinct ways to which correspond three critical stresses that can be computed analytically. The first possibility [Fig. 1(a)] is that the segment, when bowing out, *meets* a new obstacle (n'), in which case the segment is cut in two in order to incorporate the new obstacle on the dislocation. The potential obstacle is found by searching the obstacles that are in the half-circle of diameter equal to ℓ^*_{SF}, the distance between n_S and n_F. The first obstacle that the dislocation will meet corresponds to the maximum radius of curvature R^*_{meet} and the stress is $\tau^*_{meet}=1/2R^*_{meet}$. The second possibility [Fig. 1(b)] is that the segment becomes *unstable* if its shape

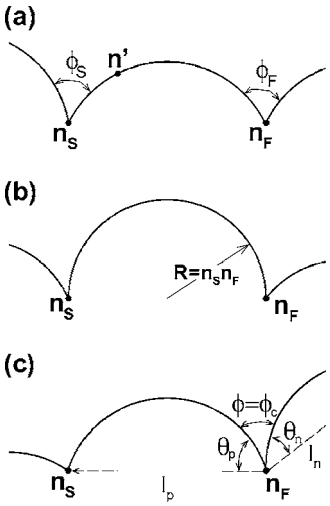

FIG. 1. Sketch of the three evolution mechanisms for a dislocation segment: (a) meet a new obstacle, (b) become unstable, and (c) break an obstacle (right-hand obstacle in the present sketch).

reaches a half-circle. Its radius of curvature is then $\ell^*_{SF}/2$ and the corresponding stress is the segment Orowan stress: $\tau^*_{Orowan}=1/\ell^*_{SF}$. The obstacle (either n_S or n_F) around which the dislocation makes the smallest angle is declared *broken*, which leads to the third case. In this case [Fig. 1(c)], one of the angles (ϕ_S or ϕ_F) becomes smaller than ϕ_c and the corresponding obstacle is *broken*. Both segments pinned at this obstacle are removed and replaced by a single segment. With the notations of Fig. 1(c) where $\vec{\ell}_p$ and $\vec{\ell}_n$ are the vectors joining the broken obstacle to its two neighbors on the dislocation line and θ_p and θ_n the corresponding angles, the obstacle breaks if

$$\phi=\phi_c=2\pi-\alpha_0-\theta_p-\theta_n, \tag{4}$$

where $\cos(\alpha_0)=\frac{\vec{\ell}_p\cdot\vec{\ell}_n}{\ell_p\ell_n}$, $\sin(\theta_p)=\tau^*_{break}\ell^*_p$ and $\sin(\theta_n)=\tau^*_{break}\ell^*_n$. By simple algebra, it can be shown from the above equation that

$$\tau^*_{break}=\frac{|\sin(\alpha_0+\phi_c)|}{\sqrt{2\cos(\alpha_0+\phi_c)\ell^*_p\ell^*_n+\ell^{*2}_p+\ell^{*2}_n}}. \tag{5}$$

In this third case, a search is made for nonbroken obstacles in the area below the new segment, in which case the segment is subdivided in order to incorporate these obstacles on the dislocation.

B. Evolution algorithm

The evolution algorithm is based on a *dynamical* assumption: the event that occurs first is the one with the smallest associated stress. Thus a segment on the dislocation will evolve by the mechanism of smallest stress among τ^*_{meet}, τ^*_{Orowan}, and τ^*_{break}. We call this stress the *event stress* τ^*_{event}. Then, still according to our dynamical assumption, the dislocation configuration will evolve by the event corresponding to the minimum event stress among all segments: $\tau^*_{min}=\min(\tau^*_{event})$.

Suppose that the dislocation is in a stable configuration at a given applied resolved shear stress τ_A^*, i.e., the event stresses of all the segments are larger than τ_A^* (at the beginning of the simulation, the dislocation is at the bottom of the cell in contact with a single obstacle and $\tau_A^*=0$). The applied stress is increased up to the lowest event stress among all segments. The segment associated to this stress is forced to evolve according to the corresponding mechanism, which modifies the event stresses of its first neighbors. A new event is realized without changing the applied stress if the new lowest event stress τ_{min}^* is still lower than the applied stress. A succession of events may therefore occur at fixed applied stress (which physically corresponds to the unzipping mechanism) as long as at least one segment has an event stress lower than τ_A^*. Two cases are then possible. Either the dislocation reaches the top of the simulation cell, in which case the applied stress is the CRSS, or the dislocation finds a new stable configuration. In this latter case, the algorithm is iterated and the applied stress increases up to the new τ_{min}^*.

C. Boundary conditions

We mainly applied periodic boundary conditions along the dislocation line, but also tested mirror boundaries as in Ref. 6. In summary, we found that mirror boundaries lead to higher CRSS but that the finite size effects are similar to those obtained with periodic boundaries. We also observed a dispersion of the CRSS higher with mirror conditions. The reason for the higher stresses is that with mirror boundaries, the unzipping process stops at the mirror planes while with periodic boundaries, it can propagate to the other side of the cell, come back, and proceed further. Moreover, mirror boundary conditions lead to strong obstacles on the borders of the cell whenever two obstacles close to each other are placed near a boundary and form a close quadruple with their mirror images, which is usually a defect of strong resistance.

III. SIMULATION RESULTS

Using the above computational model, we studied the dependence of the CRSS on the cell height H, the cell width W, and the breaking angle ϕ_c. H is also the dislocation glide distance and W the dislocation length. In order to limit uncertainties on the calculated CRSS below 0.5%, we performed 160 simulations for each triplet of parameters. Figure 2 shows the yield stress as a function of the cell height for different cell widths and for two breaking angles, $\phi_c=170°$ and 177°. In order to compare obstacles with different breaking angles, we normalize the yield stress by that given by Friedel's law [Eq. (2)].

As expected from the qualitative arguments presented in the Introduction, the CRSS increases with the cell height H because the glide distance increases and decreases when the cell width W increases because the dislocation length increases. We also note that the normalized yield stress is larger for weaker obstacles, i.e., the difference between the simulation results and Friedel's law increases when the obstacle resistance decreases.

We identified the parameters that determine this finite size effect. First, we expect the yield stress not to depend on the absolute cell width W but rather on the average number of obstacles along the dislocation line. This number is estimated by the ratio between the cell width W and the average distance between obstacles l_F predicted by Friedel's law [Eq. (1)], which yields

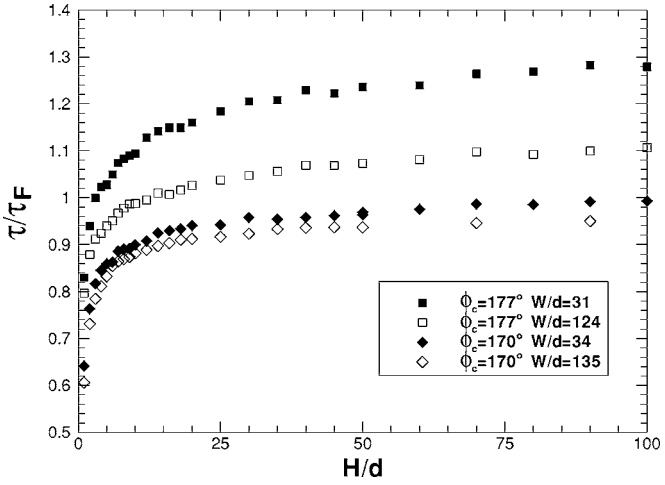

FIG. 2. Yield stress [normalized by Friedel's stress, Eq. (2)] as a function of the glide distance $H^*=H/d$, for different dislocation lengths $W^*=W/d$ and breaking angles noted in the figure.

$$n_w = W^* \sqrt{\cos(\phi_c/2)}. \tag{6}$$

Second, we expect the yield stress not to depend on the absolute glide distance H, but rather on the number of obstacle configurations met by the dislocation during its glide through the cell. Since the obstacle resistances considered here are low, the dislocation is almost straight. It is approximately located in a band of height h, the deflexion made by the dislocation pinned between two obstacles separated by the average distance l_F. The number of configurations tested is then estimated by the ratio between the cell height H and $h=\sqrt{\cos(\phi_c/2)}d/4$, which yields

$$n_h = 4\frac{H^*}{\sqrt{\cos(\phi_c/2)}}. \tag{7}$$

Figure 3 shows the yield stress as a function of the number of configurations tested n_h for various numbers of obstacles on the dislocation line n_w. The simulations compiled in this figure were performed with breaking angles from 160° to 177°. We see that the data fall on master curves that depend only on n_w, which confirms that the two parameters discussed above are those controlling the finite size effect. We again see that the CRSS increases with n_h and decreases with n_w.

Figure 3 shows that for large values of both n_w and n_h, the CRSS converges to about $0.9\tau_F$ as expected from the statistical models proposed in Refs. 7 and 8 for infinitely large arrays. More precisely, the CRSS extrapolated for infinite values of n_h can be accurately fitted by the following expression:

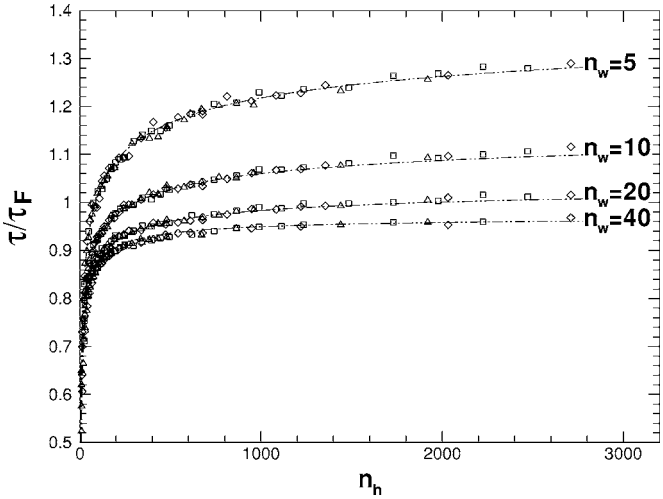

FIG. 3. Scaled yield stress as a function of the number of obstacle configurations in the glide direction n_h for different average numbers of obstacles on the dislocation line n_w. This figure is a compilation of simulations carried out with critical breaking angles ranging from 160° to 177° to which correspond different symbols.

$$\tau_0^*(n_w) = \tau_\infty^* \left(1 + \frac{3.77}{n_w}\right) \tag{8}$$

with $\tau_\infty^* = 0.89\tau_F^*$, the infinite array limit. For small values of n_w (e.g., 5), the CRSS is about 50% above τ_∞^* with a slow, if any, convergence when the glide distance n_h increases. Also, for low n_h (typically $n_h < 200$), the CRSS drops below Friedel stress and converges to 0 as n_h goes to 0. With mirror boundary conditions, similar results were obtained with $\tau_0^*(n_w) = 0.91\tau_F^*(1+4.5/n_w)$.

We also considered square arrays as in most previous studies.[6,9,12] In this case, for a given breaking angle, the CRSS is a function of $W^* = H^*$ and thus a function of $W^*H^* = WH/d^2$ which is the expected number of obstacles in the simulation cell. We thus considered a cell of fixed size and performed simulations with different numbers of obstacles. It is equivalent to considering a cell of varying size with a constant obstacle density. The result is shown in Figure 4 for different breaking angles. The particularity of this square geometry is that when the number of obstacles in the glide direction increases, the number of obstacles on the dislocation line and the number of obstacle configurations increase at the same time. Fig. 4 shows that the overall effect is a decrease of the CRSS. The softening effect due to the increase of the dislocation length is thus stronger than the hardening effect due to the corresponding increase in the glide distance. The divergence for small obstacle numbers is more marked for weaker obstacles and also, for weaker obstacles, larger cells are required to reach convergence.

The present results cannot be fitted by the Labusch formula for finite size effects[8] in particular because the latter cannot be cast into a function of only n_w and n_h. The dash-dotted curves in Figs. 3 and 4 are from a nonphysical, though very accurate, fit expressed as

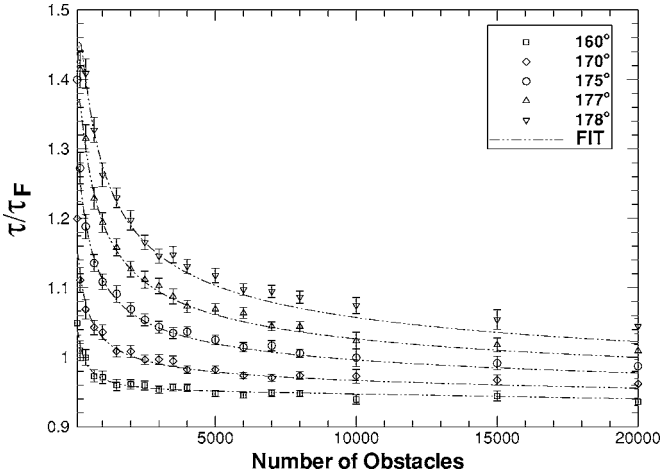

FIG. 4. Scaled yield stress as a function of the number of obstacles in a square simulation cell of fixed unit size. The breaking angles considered are noted in the figure. Statistical error bars are shown.

$$\tau^* = \tau_0^*(n_w)\left(1 - \frac{a/n_w + b + cn_w + dn_w^2}{n_h^{en_w+f}}\right) \tag{9}$$

with $a=1.079$, $b=0.663$, $c=-0.00246$, $d=0.000853$, $e=0.0122$, and $f=0.141$.

IV. DISCUSSION

A. Analogy with branching processes

The finite size effect discussed here can be analyzed using the analogy with *Branching Processes* first proposed by Hanson and Morris,[7] according to which a stable configuration with n obstacles on the dislocation line can be viewed as a surviving branching process of n generations. The initial individual is an obstacle taken on one side of the array. The first generation (*off-springs*) consists of mechanically stable obstacles found in the area A^* swept around the initial obstacle by rotating a circle of radius R^* through an angle equal to a fraction of $\pi - \phi_c$ (this fraction is chosen in order to satisfy the boundary conditions, see Ref. 7 for details). Each off-spring will itself have a random number of children in the next generation. A stable configuration is obtained if the number of off-springs remains nonzero for n generations, meaning that at least one dislocation was constructed with n stable obstacles along its line. Since the obstacles are randomly distributed in the glide plane, the probability of finding m obstacles in an area A^* is Poisson-distributed:

$$P_{A^*}(m) = \frac{(A^*)^m}{m!}\exp(-A^*). \tag{10}$$

Hanson and Morris[7] used the extinction theorem of infinite arrays to prove that in this limit, stable configurations exist only if $A^* \leqslant 1$. The case $A^* = 1$ corresponds to the infinite array CRSS τ_∞^*. Since A^* is proportional to R^{*2} and thus to $1/\tau^{*2}$, we obtain $A^* = (\tau_\infty^*/\tau^*)^2$.

For finite sized arrays, generating functions can be used.[16] The generating function of the Poissonian process discussed above is

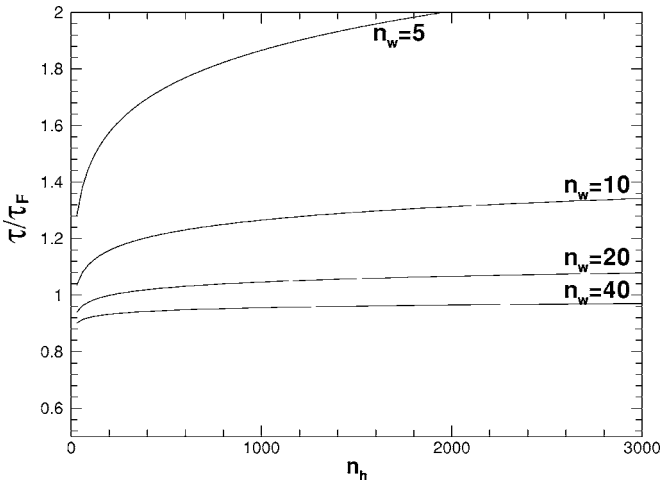

FIG. 5. Scaled yield stress as a function of n_h for various n_w predicted from a model based on branching processes.

$$\Phi_{A^*}(y) = \sum_{m=0}^{\infty} P_{A^*}(m) y^m = \exp[A^*(y-1)]. \tag{11}$$

If we note Z_n the number of off-springs in generation n and $\rho = P_{A^*}(0) = \exp(-A^*)$ the probability of finding no obstacle in the area A^*, the probability that $Z_n = 0$ is expressed as

$$P(Z_n = 0) = P(Z_{n-1} = 0) + P(Z_{n-1} = 1)\rho + P(Z_{n-1} = 2)\rho^2 + \cdots = \Phi_{Z_{n-1}}(\rho), \tag{12}$$

where Φ_{Z_n} is the generating function of Z_n, which is expressed as $\Phi_{Z_n}(y) = \Phi_{A^*}\{\Phi_{A^*}[\cdots\Phi_{A^*}(y)]\}$ (n times).

Thus for a simulation cell with n_w obstacles along the dislocation line and n_h possible starting obstacles along the glide distance, the probability that the CRSS is less than a given stress τ^*, which is equal to the probability of finding no stable configuration in the cell, is

$$P(\mathrm{CRSS} < \tau^*) = (\Phi_{Z_{n_w-1}})^{n_h} \tag{13}$$

and the CRSS averaged over all realizations of the random distribution of obstacles is

$$\langle \tau^* \rangle = \int_0^{\infty} [1 - P(\mathrm{CRSS} < u)] du. \tag{14}$$

Figure 5 shows the resulting prediction for the scaled CRSS as a function of n_h. The trends are well-reproduced: the CRSS increases with n_h, tends to zero when n_h goes to zero, and diverges for $n_w = 5$. Also, we checked that in the limit of large n_h, the CRSS decreases inversely proportionally with n_w, as obtained in the simulations [see Eq. (8)]. However, the comparison remains only qualitative, since the predicted CRSSs are significantly larger than those obtained by simulations. There are several reasons for this. First, the boundary conditions are difficult to account for. They enter here only through the ratio between τ_∞^* and τ_F^* taken as 0.89. Periodic boundary conditions should have a larger effect since they strongly decrease the number of valid stable configurations that must be continuous across the sides of the cell. Also, the number of starting configurations is difficult to evaluate. It is necessarily proportional to n_h, but does not have to be equal to the latter as assumed here. We were not able to find an expression of this number that quantitatively fits the simulation results.

B. Comparison with DD simulations

The effect discussed here concerns only weak obstacle environments where the dislocation remains mostly straight during its glide. A system of particular interest is thus a solid-solution alloy where dislocations are pinned by single or small clusters of solute atoms.

We see from Figs. 2 and 4 that the difference between the estimated CRSS and its infinite array limit τ_∞^* is larger for weaker obstacles and lower densities. Indeed, in square cells (Fig. 4), the estimated CRSS can be as high as 50% above τ_∞^* for weak obstacles ($\phi_c > 175°$) in low densities (number of obstacles <1000), but it is only 10% above this limit with 20 000 obstacles. The convergence is rather slow. With stronger obstacles ($\phi_c = 160°$), the difference between the estimated CRSS and τ_∞^* is smaller: 20% with 100 obstacles down to 5% with 20 000 obstacles.

Interestingly, Fig. 3 shows that in rectangular cells, for a given number of obstacles along the dislocation line (n_w), increasing the glide distance will not lead to the infinite array limit τ_∞^* but to an overestimated CRSS that can be as high as 50% above τ_∞^* for small values of n_w. Square cells appear to be more adapted because in this geometry, when the cell size increases at a given obstacle density, or equivalently, when the obstacle density increases at a given cell size, n_w and n_h increase simultaneously and the two opposite effects of strengthening due to the variation of n_h and softening due to n_w balance each other and lead to a convergence of the CRSS to the infinite array value.

In dislocation dynamics simulations,[17–19] the number of obstacles rarely exceeds 1000 because of the computational load associated to such simulations. However, strong obstacles are usually considered (up to nonshearable particles with $\phi_c = 0$) for which the finite size effect discussed here is small. In fact, with strong obstacles, the geometry of dislocation motion changes. The dislocation is no more straight but follows finger paths in order to take advance of weaker regions in the array of strong obstacles.[6] Unzipping events can no longer propagate along the entire length of the dislocation. Note that finite size effects are also expected in this case since the distribution of weak regions will also be statistical and will depend on the cell size.

V. CONCLUSION

We employed a line tension model to study finite size effects in the glide of dislocations in a random environment of weak obstacles. This model, though very simplified, retains the main physical ingredient, i.e., the unzipping mechanism. This study confirms the accuracy of Friedel's law, with a CRSS for an infinite dislocation with an infinite glide distance equal to $0.89\tau_F$. However, the present study shows that

with finite dislocations and/or finite glide distances, the CRSS is overestimated with respect to this limit, except for very small glide distances. In particular, increasing the glide distance while keeping a constant dislocation length leads to a CRSS that converges to a value larger than the infinite array limit. We also showed that a square simulation cell leads to convergence because in this geometry the dislocation length and glide distance increase simultaneously. The present study concerns only weak obstacles, with critical breaking angles larger than 160°, in which case the dislocation remains mostly straight in its glide. Usually, stronger obstacles are considered in dislocation dynamics simulations. It could, however, become of importance in small-scale structures, such as nanocrystals made of alloys in solid solutions, where both the dislocation length and the glide distance are limited.

[1] E. O. Hall, Proc. Phys. Soc. London, Sect. B **B64**, 747 (1951).
[2] N. Petch, J. Iron Steel Inst., London **174**, 25 (1953).
[3] E. Rodary, D. Rodney, L. Proville, Y. Bréchet, and G. Martin, Phys. Rev. B **70**, 054111 (2004).
[4] L. Proville, D. Rodney, Y. Bréchet, and G. Martin, Philos. Mag. **86**, 3893 (2006)
[5] J. Friedel, *Dislocations* (Pergamon Press, Oxford, 1964).
[6] A. Foreman and M. Makin, Philos. Mag. **14**, 911 (1966).
[7] K. Hanson and J. Morris, J. Appl. Phys. **46**, 983 (1975).
[8] R. Labusch, J. Appl. Phys. **48**, 4550 (1977).
[9] J. Morris and D. Klahn, J. Appl. Phys. **45**, 2027 (1974).
[10] A. Foreman and M. Makin, Can. J. Phys. **45**, 511 (1967).
[11] M. Hiratani and V. Bulatov, Philos. Mag. Lett. **84**, 461 (2004).
[12] S. Altintas and J. Morris, Acta Metall. **34**, 801 (1986).
[13] M. Dong, M. C. Marchetti, A. A. Middleton, and V. Vinokur, Phys. Rev. Lett. **70**, 662 (1993).
[14] S. Brazovskii and T. Nattermann, Adv. Phys. **53**, 177 (2004).
[15] M. Verdier, M. Fivel, and I. Groma, Modell. Simul. Mater. Sci. Eng. **6**, 755 (1998).
[16] T. Harris, *The Theory of Branching Processes* (Dover Publications, New York, 1989).
[17] V. Mohles, Philos. Mag. A **81**, 971 (2001).
[18] T. Pretorius and E. Nembach, Acta Mater. **49**, 1971 (2001).
[19] V. Mohles and B. Fruhstorfer, Acta Mater. **50**, 2503 (2002).